IEEE Access
Multidisciplinary | Rapid Review | Open Access Journal

Received March 12, 2019, accepted April 23, 2019, date of current version May 7, 2019.

Digital Object Identifier 10.1109/ACCESS.2019.2913497

Improving the Rotational Stiffness of Compact Aerostatic Guideway by Micro-Structures Optimization

ZHONG-PU WEN, JIAN-WEI WU, YIN ZHANG, JI-WEN CUI, AND JIU-BIN TAN

Centre of Ultra-Precision Optoelectronic Instrumentation Engineering, Harbin Institute of Technology, Harbin 150001, China
Key Laboratory of Ultra-Precision Intelligent Instrumentation, Ministry of Industry and Information Technology, Harbin Institute of Technology, Harbin 150080, China

Corresponding author: Jian-Wei Wu (wujianwei@hit.edu.cn)

This work was supported in part by the National Natural Science Foundation of China under Grant 51675136, in part by the National Science and Technology Major Project under Grant 2017ZX02101006-005, and in part by the Heilongjiang Natural Science Foundation under Grant E2017032.

ABSTRACT To meet the requirement for the exact computation of rotational stiffness, this paper puts forward a mesh adaptation based analysis method for a compact multi-throttle aerostatic guideway and its constituent micro-structure. Contrary to previous methods that substituted or even ignored them, the dimensionless thickness pertaining to the depth of the micro-structure is restored and incorporated into each computational grids. The mesh adaptation procedures accept the dimensionless thickness as an intermediate variable for the target mesh and apply local modifications to adapt the mesh to match the specified size. Then, the varying regularity of rotational stiffness by micro-structures can be studied by k-ε turbulence model when tilt. The tilt angle, although small, leads to a wedge-shaped film and then an uneven pressure distribution which has been also taken into consideration. Guided by the mesh adaptation method, a vertical compact guideway with high rotational stiffness of 7.22×10^3 Nm/rad is designed and manufactured for photolithography. The experiments verify its practical accuracy and effectiveness.

INDEX TERMS Compact aerostatic guideway, mesh adaptation, multi-throttle, rotational stiffness.

I. INTRODUCTION

Aerostatic guideways and bearings, characterized by high accuracy in motion and almost no wear, have been applied widely to ultra-precision machine tools and measurement equipment [1]–[3]. In recent years, the throttling mode and structure of aerostatic lubrication have been investigated thoroughly. Orifice throttling is widely used, because of the ease of implementation and excellent characteristics [4], [5]. However, it has the disadvantage that stiffness and stability often present a mutual tradeoff [6], [7]. Presently, multi-throttle is proposed to circumvent this limitation. The aerostatic guideway used in photolithography is considered as an illustrative example. This equipment consists of several cantilevers that need to meet the requirements of high frequency, speed, acceleration and precision. And the corresponding optical structures make the aerostatic guideway compact. The use of multi-throttle is expected to achieve it, but the rotational stiffness needs to be further improved. Moreover, the quantitative effect of the micro-structures is not very clear.

Universally, the carrying capacity of a multi-throttle aerostatic guideway is studied based on the laminar models, containing the Reynolds equations. On this basis, it is convenient to obtain the analytic expression of pressure, speed and Reynolds number. Then, combining empirical formula and coefficient derived from experimentation, the study on carrying capacity achieves more convincing interoperability, especially for the infrastructure parameter design [8], [9]. It's because the assumption for simplification in laminar calculation and the homogenization effect of pressure extension are unified in the results. Nakamura and Yoshimoto [10], [11] investigate the static tilt characteristics of aerostatic bearings by laminar method theoretically and experimentally. In their study, the double row restrictors is proposed to improve the tilt stiffness of both pitch and roll directions. Zhang [12] solve the laminar boundary-layer equations to investigate the pressure depression in aerostatic thrust bearing by the method of separation of variables (MSV). For the

The associate editor coordinating the review of this manuscript and approving it for publication was Bora Onat.

further calculation, the numerical method is proposed to research the pressure extension along the micro-structures. Yadav and Sharma [13] analyzed the influence of the tilt parameter having different geometric shapes of recesses on the static and dynamic performance characteristic, by using an iterative finite element method (FEM) formulation. Pascal, Martin and Jonathan [15] provided a Lagrangian finite element method for local mesh improvement operations with a high-quality tetrahedral discretization. Eleshaky [14] use the finite volume method (FVM) to not only analyze the velocity and pressure along the direction of film thickness, but also establish turbulence equations to govern the three-dimensional flow. Chen [16] use the resistance network method (RNM) to design an aerostatic rectangular bearing with X-shaped grooves. No matter which method, constructing an effective mesh of multi-throttle has been recognized as an important problem in computational fluid dynamics (CFD) [17].

In order to study the varying regularity of rotational stiffness by micro-structures, it is necessary to confirm laminar-turbulent transition zones. As for this complex flow adjacent to the superposition of macro- and micro-structures, a boundary mesh independent on the features of the walls is required. Thus, this paper puts forward a mesh adaptation based analysis method to investigate the effect of the micro-structures on the carrying performance. The mesh adaptation procedures accept the dimensionless quantities, derived from the depth and thickness of the micro-structures, as input for the target mesh and apply local mesh modifications to adapt the mesh to match the specified size. Thus, the boundary layer meshes are restricted by the parameters of micro-structures and tilt. Guided by the mesh adaptation method above, the vertical aerostatic guideway in the exposure system of the photolithography is redesigned after the micro-structure optimization. Experiments verify the practical accuracy and effectiveness of the mesh adaptation method.

II. THE ANALYSIS MODEL OF MULTI-THROTTLE AEROSTATIC GUIDEWAY WITH MICRO-STRUCTURES

A. THE MODEL OF THE MULTI-THROTTLE AEROSTATIC GUIDEWAY

The exposure system of photolithography and 3D model of the vertical guideway being studied is shown in Fig. 1. When the motor drives the diaphragm by the guide sleeve T and cantilever upwards (or downwards) with acceleration, the torque will produce clockwise (or counter clockwise) rotation tendency in the *Y-Z* plane. Therefore the compact guideway needs to provide an impedance tilt moment to resist rotation. The impedance tilt moment is mainly provided by two structurally symmetric surfaces denoted as M. Therefore, the rotational stiffness of the wedge-shaped air film directly decides the position and motion accuracy. Harder still, the macro-structure (infrastructure) and operating condition of the guideway are limited by the application background.

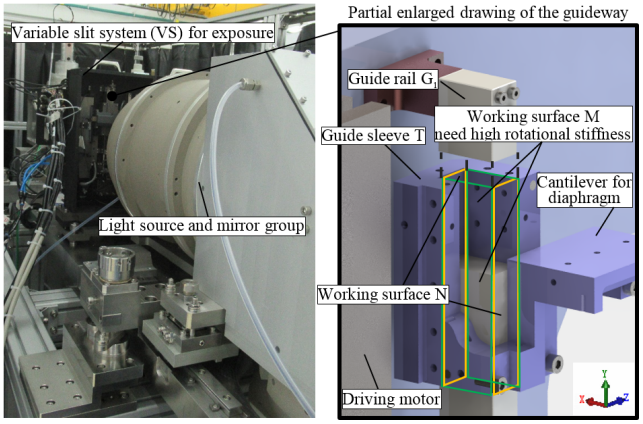

FIGURE 1. The exposure system of photolithography and 3D model of the vertical guideway being studied.

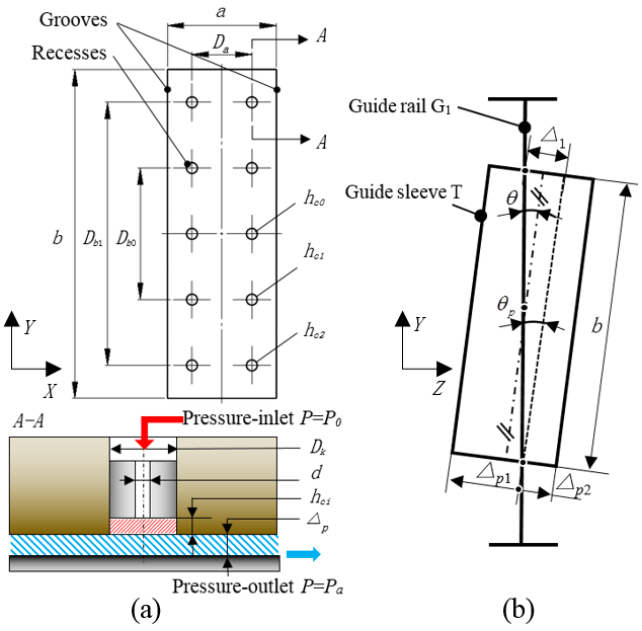

FIGURE 2. Analysis models of the multi-throttle aerostatic guideway with recesses and grooves. (a) Model of surface M. (b) Model of tilt.

TABLE 1. Dimensions of the aerostatic guideway with inherent.

Parameters	$a\times b$ (mm×mm)	D_k (mm)	d (mm)	Δ_p (μm)	Δ_{pi} (μm)	P_0 (atm)
Value	20×60	2	0.2	9	from 2 to 16 along with θ	4

Thus, the load capacity and rotational stiffness of a compact guideway can be improved by micro-structure such as providing a ring of shallow recesses around the orifices, corresponding with decompression grooves for stability or other micro-structures, as shown in Fig. 2. There h_{ci} is defined as the depth of recesses, D_a and D_{bi} are the separation distances between recesses and θ is the tilt angle. Table 1 shows the dimensions of the compact guideway with inherent.

Because of the air film width a is about 10^3 times larger than its thickness Δ_p and the depth of recesses h_{ci}, a simplified and equivalent structure of the decompression grooves

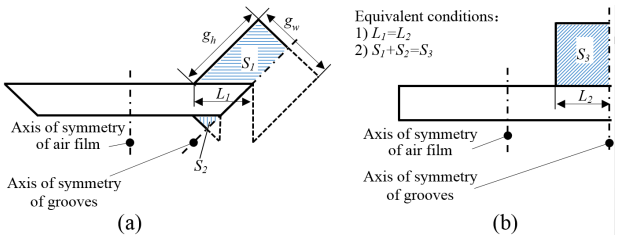

FIGURE 3. The equivalent structure of groove. (a) Actual structure. (b) Simplified structure for practical modeling.

are adopted for practical modeling, as shown in Fig. 3. There g_w is defined as the width of grooves and g_h is the depth of grooves.

At the boundary of the pressure-outlet, hydraulic diameter D_{Hi} is defined as: $D_{Hi} = 2\Delta_{pi}$.

At the boundary of the pressure-inlet, hydraulic diameter D_H is defined as: $D_H = d$

The tilt angle θ of the guide sleeve is regarded as an independent variable in the model, characterized by the difference between the thickness of air films Δ_{p1} and Δ_{p2}, as:

$$\theta = \theta_p = \arctan\frac{\Delta_1}{b} \tag{1}$$

where, $\Delta_1 = \Delta_{p1} - \Delta_{p2}$ and $2\Delta_p = \Delta_{p1} + \Delta_{p2}$

Here, the tilt moment M_r generated by two surfaces M is the dependent variable, given by:

$$M_r = 4\left(\iint P(x,y)dS_M\right)\cdot L_d \tag{2}$$

Then, the rotational stiffness K_θ of the aerostatic guideway is given by:

$$K_\theta = \frac{\partial M_r}{\partial\theta} \tag{3}$$

NOMENCLATURE

F	carrying capacity
M_r	tilt moment
P	pressure
R	gas constant
T	absolute temperature
η	kinetic viscosity
μ	molecular viscosity
μ_t	turbulent eddy-viscosity
k	turbulent kinetic energy
ε	dissipation rate of k
κ	thermal conductivity
u^+	dimensionless velocity
u_i, $u_i^{'}$	mean and fluctuating time-averaged velocity components
y_{min}	actual minimum thickness
y^+_{min}	dimensionless minimum thickness
g_w	width of grooves
g_h	depth of grooves
h_{ci}	depth of recesses
Δ_p	average thickness of pressure-outlet
Δ_{pi}	thickness of pressure-outlet
Δ_q	difference of thickness in Exp.
Δ_{q0}	difference of thickness at no-load
Δ_1	difference of thickness in CFD
Δ_2	relative altitude in Exp.
θ_p	inclination angle in CFD
θ_q	inclination angle in Exp.
c_p	constant-pressure specific heat
M^j	topological mesh entities of dimension j. (j=0: vertex, j=1: edge, j=2: face, j=3: region)
M^j_t	the t times mesh entity of dimension j.

Due to the symmetry of the structure and the boundary conditions, only half of the designed aerostatic surface S_M is under consideration. The $P(x, y)$ is the pressure value corresponding to any finite volume node (x, y) on the S_M. By mesh adaptation method, the pressure distribution $P(x, y)$ and the eccentricity L_d can be obtained with varying parameters of micro-structures, such as h_{ci}, g_w and g_h.

B. THE METHOD OF ANALYSIS FOR ROTATIONAL STIFFNESS

1) GOVERNING EQUATIONS

In the irregular narrow fluid domain, laminar-turbulent transition zones should be confirmed for turbulent computation. Sharp turnings, adverse pressure gradients and other localized flow fields will be formed near the micro-structures. To represent this complicated flow-field, Navier–Stokes equations for three-dimensional and compressible flow is being solved for turbulence. The indicial notation form in the Cartesian coordinates is given by:

$$\frac{\partial(\rho u_i)}{\partial x_i} = 0 \tag{4a}$$

$$\frac{\partial(\rho u_i u_j)}{\partial x_j} = -\frac{\partial P}{\partial x_i} + \frac{\partial}{\partial x_j}\left[\mu\left(\frac{\partial u_i}{\partial x_j} + \frac{\partial u_j}{\partial x_i} - \frac{2}{3}\delta_{ij}\frac{\partial u}{\partial x}\right)\right] - \frac{\partial\left(\rho\overline{u_i' u_j'}\right)}{\partial x_j} \tag{4b}$$

$$\frac{\partial}{\partial x_j}\left\{u_j\left[c_p\frac{P}{R} + \frac{\rho}{2}\left(u_1^2 + u_2^2 + u_3^2\right)\right]\right\} = -\frac{\partial}{\partial x_j}\left[\left(\kappa + \frac{c_p\mu_t}{0.85}\right)\frac{\partial T}{\partial x_j} + u_i(\mu + \mu_t)\left(\frac{\partial u_i}{\partial x_j} + \frac{\partial u_j}{\partial x_i} - \frac{2}{3}\delta_{ij}\frac{\partial u}{\partial x}\right)\right] \tag{4c}$$

with $i = 1, 2, 3$ and $j = 1, 2, 3$ represent properties in Y, Z, X directions, respectively. The Reynolds stress tensor in Eq. (4b) is given by:

$$\rho\overline{u_i' u_j'} = \frac{2}{3}\left(\rho k + \mu_t\frac{\partial u_i}{\partial x_i}\right)\delta_{ij} - \mu_t\left(\frac{\partial u_i}{\partial x_j} + \frac{\partial u_j}{\partial x_i}\right) \tag{5a}$$

where, δ_{ij} is the Kronecker delta symbol which is equal to unity when $i = j$ and zero when $i \neq j$. The molecular

viscosity μ is calculated from the Sutherland's law. And the merge item of $\frac{\partial u}{\partial x}$ is given by:

$$\frac{\partial u}{\partial x} = \frac{\partial u_i}{\partial x_i} + \frac{\partial u_j}{\partial x_j} \tag{5b}$$

2) TURBULENCE CLOSURE

In this paper, turbulence is modeled by using the realizable $k-\varepsilon$ model. The turbulent eddy viscosity is computed according to the relation:

$$\mu_t = \rho C_\mu \frac{k^2}{\varepsilon} \tag{6}$$

with the coefficient C_μ no longer constant. The transport equations modeled for k and ε in the realizable k-ε model are:

$$\frac{\partial}{\partial t}(\rho k) + \frac{\partial}{\partial x_j}(\rho k u_j) = \frac{\partial}{\partial x_j}\left[(\mu + \mu_t)\frac{\partial k}{\partial x_j}\right] + \mu_t S^2 - \rho\varepsilon\left(1 + \frac{2k}{a_c^2}\right) \tag{7a}$$

$$\frac{\partial}{\partial t}(\rho \varepsilon) + \frac{\partial}{\partial x_j}(\rho \varepsilon u_j) = \frac{\partial}{\partial x_j}\left[\left(\mu + \frac{\mu_t}{1.2}\right)\frac{\partial \varepsilon}{\partial x_j}\right] + 0.43\rho S\varepsilon - 1.9\rho\frac{\varepsilon^2}{k + \sqrt{\mu\varepsilon}} \tag{7b}$$

where, S is the modulus of the mean rate-of-strain tensor, defined as $S = \sqrt{2S_{ij}S_{ij}}$ and a_c is the speed of sound. The constants in the above equations have been established to ensure that the model performs well for certain coupled flows [18].

3) MESH ADAPTATION

The governing equations above can incorporate dimensionless quantities representing the depth and thickness of the micro-structures, and then quantify the effect of the micro-structures and small inclination angle on the carrying performance. The dimensionless velocity u^+ at the micro-structures is modified as a mixed function of the linear wall law associated with laminar flow and the logarithmic law associated with turbulent flow as follows:

$$u^+ = e^{\Gamma} u^+_{lam} + e^{1/\Gamma} u^+_{turb} \tag{8}$$

The mixing coefficient is:

$$\Gamma = -\frac{C_a (y^+)^4}{1 + C_b y^+} \tag{9}$$

where, $C_a = 0.01$ and $C_b = 5$.

As the term correlating the local flow field and the fluid domain, the use of u^+ needs corresponding high-quality mesh. According to the principle that the first interior node is placed the viscous boundary layer, the actual thickness y is set up. The dimensionless thickness y^+ and actual thickness y are related as:

$$y = \frac{y^+ \eta}{\rho u_\tau} \tag{10}$$

where the shear rate, shear stress and coefficient of friction are, respectively:

$$u_\tau = \sqrt{\frac{\tau_w}{\rho}},\ \tau_w = C_f \times \frac{1}{2}\rho u^2$$

and

$$C_f = 0.058 Re^{-1/5}$$

So, the actual minimum thickness can be expressed as $y_{\min}$:

$$y_{\min} = y^+_{\min}\eta/\rho u\sqrt{\frac{0.058 Re^{-\frac{1}{5}}}{2}} \tag{11}$$

Mesh adaptation procedures are used to establish the computational mesh that satisfies the y_{min} requirements above, by cyclic refinement. In each refinement step, the corresponding old-to-new entity mapping is formed. Then the links for newly entities can be effectively set up by the communication step. Each communication step is carried out after all tagged edges and faces have been split. Shewchuk [19], [20] provides thorough guide to Delaunay refinement algorithms that are guaranteed to generate meshes with high quality and puts forward an algorithm tends to generate meshes with fewer tetrahedral.

Enlightened by him, the pseudo code of the parallel refinement algorithm is given in Algorithm 1.

Algorithm 1 Pseudo Code for Mesh Refinement

```
for all M_t^j (j=1, 2) which have been tagged into buffer
N for refinement partition
    symmetric split M_t^j
    if the entity being split resides on the boundary
    layer
        for each remote copy of the current M_t^j
            pack the newly entities with the
            corresponding current M_t^j
            add M_t^j to the list of update buffer UN
        end for
    end if
end for
send out the messages in UN
repair the links of newly entities in terms of what
received
subdivide the mesh regions as in serial
```

4) ADAPTIVE LOOPS AND SIMULATION

An adaptive loop is constructed using a set of interoperable components that includes sub-regional mesh generation, modification and smoothing. The procedure links the analysis and adaptation components needed for the successful simulation on the domain, shown in Fig. 4. As shown in Fig. 4(a), hexahedral grids are employed to establish the original mesh sub-regionally to ensure easy boundary stratification and fitting. The original mesh encompasses all of

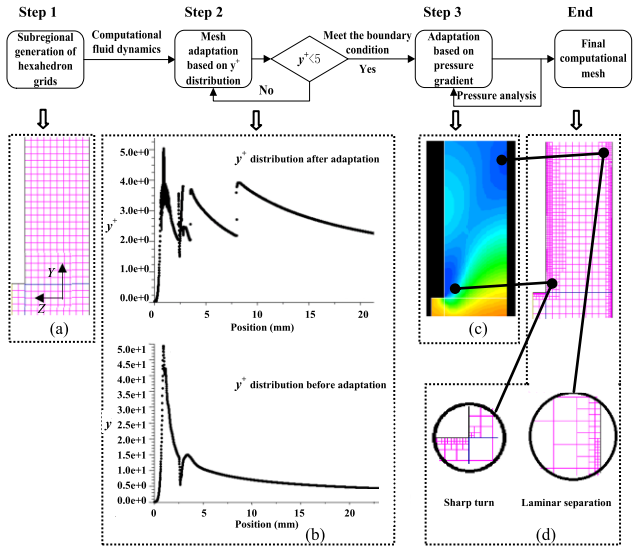

FIGURE 4. Steps of the mesh adaptation-based modeling method for calculation. (a) Partial plane of original mesh by sub-regional generation. (b) y^+ distribution before and after adaptation. (c) Partial pressure distribution after adaptation. (d) Partial plane of the final mesh.

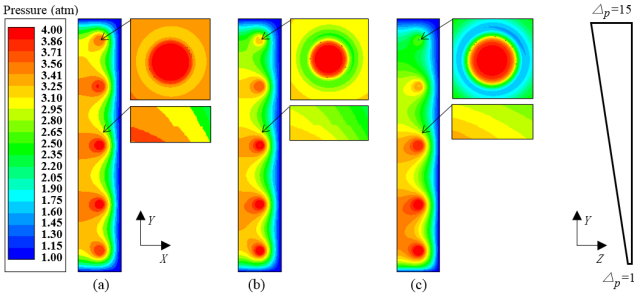

FIGURE 5. Surface pressure distribution of wedge-shaped gas film S_M. ((a), (b) and (c) are the pressure distribution of initial mesh, first adapted and second adapted mesh respectively.)

the multi-throttle structures, including the boundaries, air film, recesses, grooves and so on. The original mesh needs to be subdivided by adaptation based on the distribution of y^+ (shown in Fig. 4(b)) and pressure gradient (shown in Fig.4(c)). In these two steps, the y^+ is limited as $y^+ \leq 5$ to meet with the requirement of FVM the on the viscous bottom layer. The top graph of Fig. 4(b) shows that all the grids with points of y^+ greater than 5 have been subdivision and refinement. Fig. 4(c) shows that the mesh is captured and refined in the pseudo shock region clearly. As shown in Fig. 4(d), the final mesh can be refined at the sharp corner and the region of laminar separation by a strategy of partial capture and subdivision.

As shown in Fig. 5, the resulting pressure distribution tends to be increasingly realistic with the number of adaptations performed. The initial mesh is too coarse and these figures demonstrate its inability to capture the uneven pressure distribution of wedge-shaped gas film. Critical flow locations, including the turns around orifices and the downstream of recesses, get significantly refined.

Without any subjective modification in the process of adaptation, the degree of subdivision and the regions to be subdivided are determined in the final stage by the characteristics of computational domain. By avoiding unnecessary and excessive subdivision, the adaptation-based method can ensure mesh quality and meet the multiple requirements at the same time. Therefore, the method can effectively represent the effect of the micro-structures on computational domain, and meanwhile realize the significant computational savings over isotropic meshes of equivalent resolution.

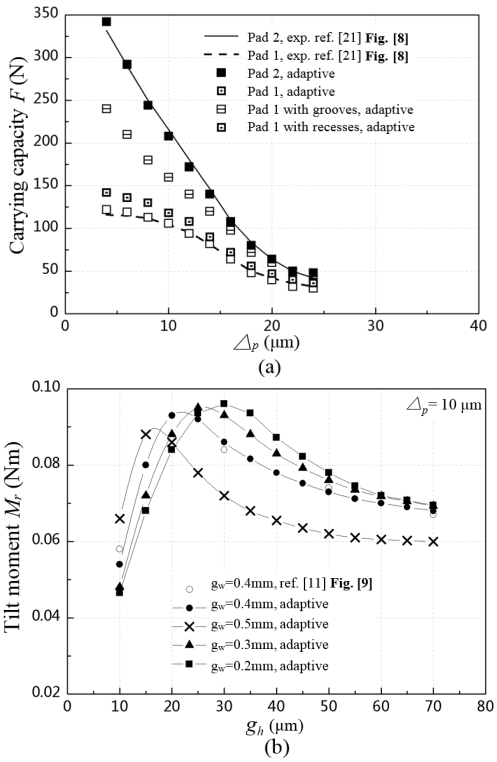

FIGURE 6. Influences of recesses and grooves on carrying capacity and tilt moment. (a) Variations of carrying capacity of 4 structures with micro-structures changing. (b) Variations of tilt moment of 4 structures with g_w changing when $\Delta_p = 10\mu$m.

C. VERIFICATIONS

To verify the adaptive method, as shown in Fig. 6, the results of adaptive simulations are compared with the experimental results in reference [21] and the results achieved by analytic method [11]. It is seen that, the results of adaptive simulations are in good agreement with the experiment and analytic method (the results of $\overline{M}/\delta$ should be transformed to equivalent to M_r).

Fig. 6(a) shows that the adaptive method can distinguish the influences of grooves and recesses on carrying capacity F. Fig. 6(b) represents the influences of groove depth g_h on the tilt characteristics M_r at different groove width g_w when $\Delta_p = 10\mu$m. It also illustrates that there exists space for the improvement tilt moment by the micro-structure optimization.

III. RESULTS AND DISCUSSIONS

The original structure M_1 of the working surface M is redesigned as a new structure M_5 to obtain a greater rotational stiffness. The differences in the parameters of the 5 structures from M_1 to M_5, including the depth of recesses h_{ci} and width of the grooves g_w, are shown in Table 2.

TABLE 2. Parameters of the 5 structures from M_1 and M_5.

Optimizing parameters		D_a (mm)	D_{b0} (mm)	D_{b1} (mm)	$h_{c0}/h_{c1}/h_{c2}$ (μm)	g_w (mm)
Value	M_1	10	28	50	30	1
	M_2				24	0.8
	M_3				18	0.6
	M_4				30/24/21	0.8
	M_5				30/18/12	0.6

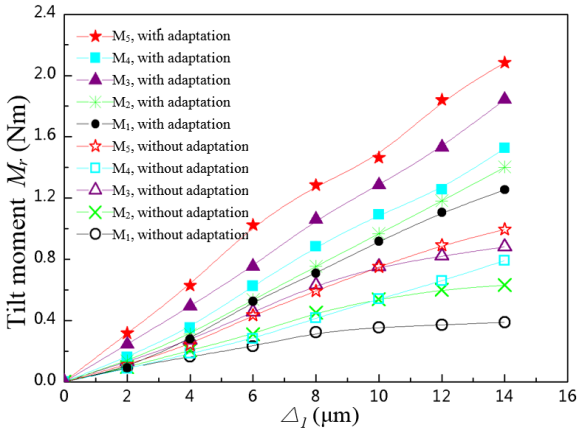

FIGURE 7. Tilt moment of the 5 structures with and without adaptation.

By the proposed modeling method, the mesh is adapted and final determined to calculate the tilt moment M_r of the working surface M, given as the top 5 curves in Fig. 7. As reference, the results by the method [14] without mesh adaptation are also given as the 5 curves at the bottom of Fig. 7. It shows that the tilt moment increases with Δ_1 and decreases with h_{ci}, coinciding well with each other on trend.

Comparatively, the conventional analysis method can hardly reach the significant changes of tilt moment, especially on smaller Δ_1. For the structures of M_1, M_2 and M_3 with uniform recesses, the effect of Δ_1 on the tilt moment is tending to be gentle. It is because the averaging effect dominates much and the pressure of wedge-shaped air films will be homogenized. In addition, the conventional analysis method can't distinguish the effect of tilt moment on uniform recesses and gradient recesses. The structure of M_5 (or M_4) provides the similar moment value as M_3 (or M_2). However, the gradient recesses distribution should result in a higher tilt moment. It is because gradient recesses can make a more significant pressure increases when Δ_{p1} decreases, and make a more significant pressure decreases when Δ_{p2} increases. The changes of pressure distribution will lead to higher moment, but the conventional method cannot get the pressure distribution exactly of the wedge-shaped air films for tilt moment calculation.

Therefore previous methods are lack of accuracy and reliability on characterizing the effect of the micro-structures and the films' difference on the tilt moment. In view of the overall situation, compared with conventional ones, the adaptation-based analysis method can be used to get more significant and accurate moment values, especially for micro-structures with inhomogeneous recesses.

Shown in Fig. 7(b), when the air film thickness at the boundary of pressure-outlet reaches the minimum value of $\Delta_p = 2\ \mu$m, the difference between the thickness of the air films reaches the maximum value of $\Delta_1 = 14\ \mu$m. In this state, M_5 provides a maximum moment $M_r = 2.084$ Nm, which is 66.2% higher than that provided by M_1 of 1.254 Nm. When $\Delta_1 = 10\ \mu$m, M_5 only provides the increases of 47.2%. Therefore, the increasing of M_r is limited by achievable value of Δ_1.

IV. EXPERIMENTAL SEARCH

A. MEASUREMENT OF TILT MOMENT

As shown in Fig. 8 (a). The guide rail G_1 is made of alloy steel 38CrMoAl, followed by surface nitriding. The guide sleeve T and guide rail G_2 are made of aluminum alloy $AlZnMgCu_{1.5}$, with the surface having undergone anodic oxidation. As shown in Fig. 8 (b), the tilt moment of M_1 and M_5 are tested under the same environment, pressure and other operating conditions as specified.

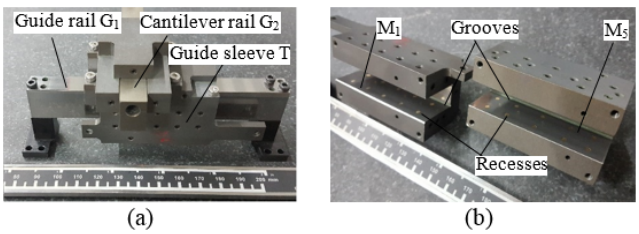

FIGURE 8. Aerostatic guideways for experiment. (a) Compact guideway of cantilevered mechanism. (b) Original structure M_1 and redesigned structure M_5 of working surface.

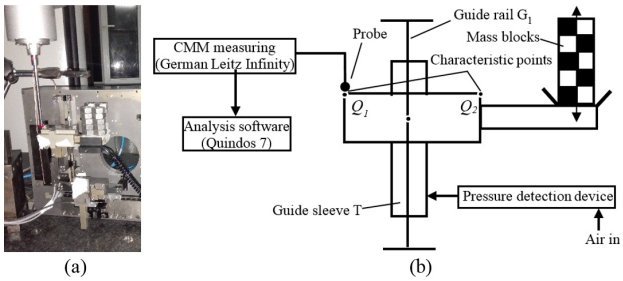

FIGURE 9. Measurement of tile moment. (a) Experimental set-up. (b) Principle of measurement.

The set-up of experimental apparatus is shown in Fig. 9(a). Unlike in the simulation, the independent variable is the

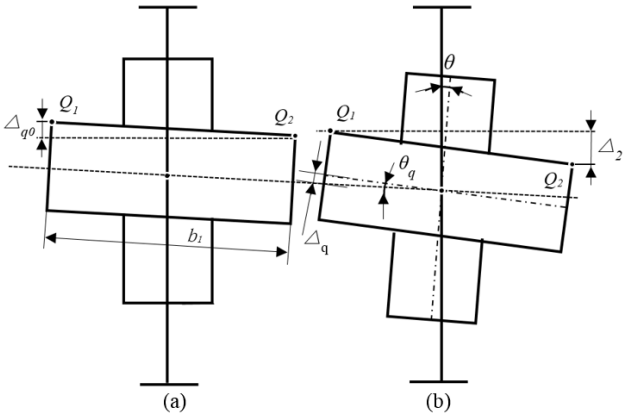

FIGURE 10. Sketch of measurement and calculation. (a) Installation error Δ_{q0} at the no-load state. (b) Relative altitude Δ_2 at the loading state.

TABLE 3. Experimental results M_r of the structure M_1 and M_5.

M_1			M_5		
Load quality M_l/g	Tilt moment M_r/Nm	Relative altitude Δ_2/mm	Load quality M_l/g	Tilt moment M_r/Nm	Relative altitude Δ_2/mm
0	-0.240	-7.75	0	-0.561	-3.45
300	0.669	-0.6	300	0.669	0.7
322	0.701	0.7	344	0.732	2.1
344	0.732	2.0	388	0.795	3.2
366	0.763	2.8	432	0.858	4.7
388	0.795	3.6	476	0.920	5.5
410	0.826	4.3	520	0.984	6.2
432	0.858	5.3	564	1.047	7.4
454	0.889	5.8	608	1.110	8.3
476	0.920	6.8	652	1.172	8.8
498	0.952	7.6	696	1.235	10.4
520	0.984	8.8	740	1.298	11.6

load quality with equal variation in the interval, accomplished by loading discrete blocks of mass. The dependent variable is the relative altitude $_2$ of the two characteristic points Q_1 and Q_2, measured by the coordinate measuring machine (CMM) probe and processed using the software package QUINDOS 7, shown in Fig. 9(b).

The sketch of measurement and calculation is shown in Fig. 10. At the no-load state, the measured relative altitude is the installation error:

$$\triangle_2 = \triangle_{q0} \tag{12}$$

At the loaded state, the angle θ and the relative altitude $\triangle_2$ have the relation:

$$\theta = \theta_q = \arctan \frac{\Delta_q}{b_1} \tag{13}$$

where, $\Delta_q = 0.5\triangle_2 - \triangle_{q0}$

The corresponding difference in the air films thickness $\triangle_1$:

$$\Delta_1 = \frac{b}{b_1} \times \Delta_q \tag{14}$$

The measured values of the moment M_r are shown in Table 3. When the state varies from no load to full load, M_5 provides the maximum moment of 1.859 Nm, which is 51.9% higher than M_1 of 1.224 Nm. In this state, the difference between the films reaches the maximum value of $\Delta_1 = 9.9\mu$m, transformed by Eq. (14).

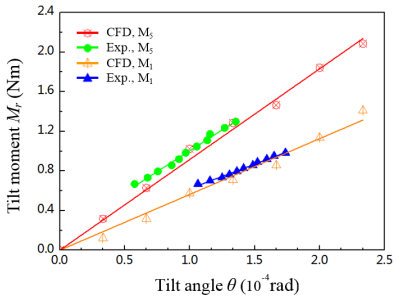

FIGURE 11. Simulation and experiment fitting stiffness of M_1 and M_5.

B. ANALYSIS OF ROTATIONAL STIFFNESS CHARACTERISTICS

The fitting stiffness of M_1 and M_5 obtained from simulation and experiment are shown in Fig. 11. Since the tilt angle of the guide sleeve T is less than 2.33×10^{-4} rad, the variation in the tilt moment can be regarded as linear. Based on this, the gradient of the fitted line can be regarded as the rotational stiffness $K_i (i = 1, 5)$ of the guideway within the range of the tilt angle. The rotational stiffness of the structure M_5 (the rake ratio) is $K_5 = 7.22 \times 10^3$Nm/rad, 47.2% higher than M_1, as obtained from adaptive simulations. This agrees well with the experiment result of 51.9%, according to the difference of the moment measured.

V. CONCLUSIONS

1. This study puts forward a new analysis method based on mesh adaptation for a multi-throttle aerostatic guideway. The method can quantify the effect of the micro-structures and small tilt angle on the carrying performance. Guided by the adaptation method, a guideway with high rotational stiffness has been designed, optimized, manufactured, and tested by relevant experiments.

2. The adaptation method can be employed to study the effect of the micro-structures and small tilt angle on the carrying performance. The results can be used to guide the design of the micro-structures for better performance. Experimental results indicate that the rotational stiffness of redesigned working surface M_5 has been increased by 47.2%, by meeting the requirement of highly accelerated motion of the guideway. Therefore, the method makes it possible to fabricate a compact aerostatic guideway for a cantilevered mechanism that is expected to facilitate high-acceleration and high-precision motion.

REFERENCES

[1] P. Yang *et al.*, "Development of high-precision micro-coordinate measuring machine: Multi-probe measurement system for measuring yaw and straightness motion error of XY linear stage," *Precis. Eng.*, vol. 35, no. 3, pp. 424–430, Jul. 2011.

[2] E. Qi, Z. Fang, T. Sun, J. Chen, C. Liu, and J. Wang, "A method for predicting hydrostatic guide error averaging effects based on three-dimensional profile error," *Tribology Int.*, vol. 95, pp. 279–289, Mar. 2011.

[3] T. Kawai, K. Ebihara, and Y. Takeuchi, "Improvement of machining accuracy of 5-axis control ultraprecision machining by means of laminarization and mirror surface finishing," *CIRP Ann.*, vol. 54, no. 1, pp. 329–332, Jan. 2005.

[4] X. Chen, H. Chen, J. Zhu, and W. Jiang, "Vortex suppression and nano-vibration reduction of aerostatic bearings by arrayed microhole restrictors," *J. Vibrat. Control*, vol. 35, no. 5, pp. 842–852, Mar. 2017.

[5] W. Ma, H. Yu, Z. Wang, L. Chen, H. Liu, and G. Zhao, "Research on characteristics of orifice type radial aerostatic bearings under high-speed condition," in *Proc. Int. Conf. Fluid Power Mechatron.*, Aug. 2011, pp. 588–592.

[6] T. Yoshimura, T. Hanafusa, T. Kitagawa, T. Hirayama, T. Matsuoka, and H. Yabe, "Clarifications of the mechanism of nano-fluctuation of aerostatic thrust bearing with surface restriction," *Tribology Int.*, vol. 48, no. 4, pp. 29–34, Apr. 2012.

[7] M. Miyatake and S. Yoshimoto, "Numerical investigation of static and dynamic characteristics of aerostatic thrust bearings with small feed holes," *Tribology Int.*, vol. 43, no. 8, pp. 1353–1359, Aug. 2010.

[8] T. Liu, Y. H. Liu, and S. J. Chen, "Design and calculation," in *Aerostatic Lubrication*, 5nd ed. Beijing, China: Harbin Institute of Technology Press, 1998, pp. 51–99.

[9] W. B. Rowe, "Basis of design procedures," in *Hydrostatic, Aerostatic and Hybrid Bearing Design*. Boston, MA, USA: Butterworth, 2012, pp. 115–125.

[10] T. Nakamura and S. Yoshimoto, "Static tilt characteristics of aerostatic rectangular double-pad thrust bearings with double row admissions," *Tribology Int.*, vol. 30, no. 8, pp. 605–611, Jul. 1997.

[11] T. Nakamura and S. Yoshimoto, "Static tilt characteristics of aerostatic rectangular double-pad thrust bearings with compound restrictors," *Tribology Int.*, vol. 29, no. 2, pp. 145–152, Feb. 1996.

[12] J. Zhang, D. Zou, N. Ta, and Z. Rao, "Numerical research of pressure depression in aerostatic thrust bearing with inherent orifice," *Tribology Int.*, vol. 123, pp. 385–396, Jul. 2018.

[13] S. K. Yadav and S. C. Sharma, "Performance of hydrostatic tilted thrust pad bearings of various recess shapes operating with non-Newtonian lubricant," *Finite Elements Anal. Des.*, vol. 87, pp. 43–55, Sep. 2014.

[14] M. E. Eleshaky, "CFD investigation of pressure depressions in aerostatic circular thrust bearings," *Tribology Int.*, vol. 42, no. 7, pp. 1108–1117, Jul. 2009.

[15] P. Clausen, M. Wicke, J. R. Shewchuk, and J. F. O'brien, "Simulating Liquids and Solid-Liquid Interactions with Lagrangian Meshes," *ACM Trans. Graph.*, vol. 32, no. 2, p. 17, Apr. 2013.

[16] M. F. Chen and Y. T. Lin, "Static behavior and dynamic stability analysis of grooved rectangular aerostatic thrust bearings by modified resistance network method," *Tribology Int.*, vol. 35, no. 5, pp. 329–338, May 2002.

[17] O. Sahni, A. Ovcharenko, K. C. Chitale, K. E. Jansen, and M. S. Shephard, "Parallel anisotropic mesh adaptation with boundary layers for automated viscous flow simulations," *Eng. Comput.*, vol. 33, no. 4, pp. 767–795, Oct. 2017.

[18] S.-E. Kim, D. Choudhury, and B. Patel, "Computations of complex turbulent flows using the commercial code fluent," in *Proc. ICASE/LaRC/AFOSR Symp. Modeling Complex Turbulent Flows*, Hampton, Virginia, pp. 259–276, 1997.

[19] R. J. Shewchuk, "Three-dimensional Delaunay refinement algorithms," in *Delaunay Refinement Mesh Generation, GER: Triangulations and Applications*. Berlin, Germany: Springer, 2006, pp. 83–123.

[20] J. R. Shewchuk and H. Si, "Higher-quality tetrahedral mesh generation for domains with small angles by constrained delaunay refinement," in *Proc. 30th Annu. Symp. Comput. Geometry*, Jun. 2014, p. 290.

[21] G. Belforte, F. Colombo, T. Raparelli, A. Trivella, and V. Viktorov, "Comparison between grooved and plane aerostatic thrust bearings: Static performance," *Meccanica*, vol. 46, no. 3, pp. 547–555, Jun. 2011.

ZHONG-PU WEN received the B.Sc. and M.Sc. degrees in instrumentation science and technology from the Harbin Institute of Technology (HIT), Harbin, China, in 2013 and 2015, respectively, where he is currently pursuing the Ph.D. degree. His research interests include aerostatic gas lubrication and computational fluid dynamics theory.

JIAN-WEI WU received the B.Sc., M.Sc., and Ph.D. degrees from the Harbin Institute of Technology (HIT), in 2004, 2006, and 2011, respectively, where he is currently an Associate Professor. His research interests include robotics and precision engineering.

YIN ZHANG received the B.Sc. and M.Sc. degrees in instrumentation science and technology from the Harbin Institute of Technology (HIT), Harbin, China, in 2015 and 2017, respectively, where he is currently pursuing the Ph.D. degree. His research interests include compliant mechanism and topology optimization theory.

JI-WEN CUI received the B.S., M.S., and Ph.D. degrees from the Harbin Institute of Technology (HIT), in 1998, 2000, and 2005, respectively, where he is currently a Professor and the Director of the Experimental Center of Optoelectronic Information. His current research interests include ultra-precision optical sensor and instrument technology.

JIU-BIN TAN received the Ph.D. degree from the Harbin Institute of Technology (HIT), Harbin, China, in 1991, where he is currently a Professor and an Academician of the Chinese Academy of Engineering. His current research interests include ultra-precision instrument engineering, and ultra-precision machining measurement equipment and technology. He received the National Invention Award of China as the first inventor, in 2006.